Size distribution dynamics reveal particle-phase chemistry in organic aerosol formation

Manabu Shiraiwa[a,b], Lindsay D. Yee[c], Katherine A. Schilling[a], Christine L. Loza[a], Jill S. Craven[a], Andreas Zuend[a,d], Paul J. Ziemann[e], and John H. Seinfeld[a,c,1]

Divisions of [a]Chemistry and Chemical Engineering and [c]Engineering and Applied Science, California Institute of Technology, Pasadena, CA 91125; [e]Air Pollution Research Center, University of California, Riverside, CA 92521; [b]Multiphase Chemistry Department, Max Planck Institute for Chemistry, 55128 Mainz, Germany; and [d]Institute for Atmospheric and Climate Science, Eidgenössische Technische Hochschule Zürich, 8092 Zurich, Switzerland

Edited by Mark H. Thiemens, University of California at San Diego, La Jolla, CA, and approved June 13, 2013 (received for review April 21, 2013)

Organic aerosols are ubiquitous in the atmosphere and play a central role in climate, air quality, and public health. The aerosol size distribution is key in determining its optical properties and cloud condensation nucleus activity. The dominant portion of organic aerosol is formed through gas-phase oxidation of volatile organic compounds, so-called secondary organic aerosols (SOAs). Typical experimental measurements of SOA formation include total SOA mass and atomic oxygen-to-carbon ratio. These measurements, alone, are generally insufficient to reveal the extent to which condensed-phase reactions occur in conjunction with the multigeneration gas-phase photooxidation. Combining laboratory chamber experiments and kinetic gas-particle modeling for the dodecane SOA system, here we show that the presence of particle-phase chemistry is reflected in the evolution of the SOA size distribution as well as its mass concentration. Particle-phase reactions are predicted to occur mainly at the particle surface, and the reaction products contribute more than half of the SOA mass. Chamber photooxidation with a midexperiment aldehyde injection confirms that heterogeneous reaction of aldehydes with organic hydroperoxides forming peroxyhemiacetals can lead to a large increase in SOA mass. Although experiments need to be conducted with other SOA precursor hydrocarbons, current results demonstrate coupling between particle-phase chemistry and size distribution dynamics in the formation of SOAs, thereby opening up an avenue for analysis of the SOA formation process.

gas–particle interactions | heterogeneous chemistry | intermediate volatility organic compounds | alkane

Laboratory chamber experiments are the basis on which gas-phase photooxidation mechanisms and subsequent formation and evolution of secondary organic aerosols (SOAs) are evaluated. Despite major advances in understanding of the mechanisms of SOA formation, the long-standing question of the relative contributions of gas- vs. particle-phase routes to SOA formation and aging for the major classes of SOA-forming hydrocarbons is still unresolved (1). Photooxidation of parent hydrocarbons and subsequent multigeneration gas-phase chemistry produce an array of semivolatile organic compounds (SVOCs) that partition into the particle phase (2, 3). At the same time, particle-phase reactions involving these condensed SVOCs can lead to formation of low-volatility compounds, such as oligomers and other high molecular mass compounds (4–6). The extent to which particle-phase chemistry is important in SOA formation for each of the major classes of SOA precursors remains unclear. We show here that the evolution of the particle-size distribution, a measurement routinely made in chamber experiments of SOA formation, holds a key to evaluating the importance of particle-phase chemistry.

Current atmospheric aerosol models underpredict ambient SOA mass (1). The missing SOAs can be partly explained by intermediate volatility organic compounds (IVOCs) that may be emitted initially as primary organic aerosol but evaporate upon dilution and are subsequently oxidized in the gas phase, yielding substantial SOA mass (7, 8). Recent modeling studies have demonstrated that IVOCs are expected to be a major precursor of SOAs in megacity outflows (9). Long-chain alkanes, mainly emitted from incomplete fuel combustion (10), constitute a substantial fraction of IVOCs. Here we use dodecane ($C_{12}H_{26}$), a surrogate compound for IVOCs, to study the connection between the chemical mechanism of SOA formation and the evolution of the size distribution.

Results and Discussion

Dodecane Photooxidation Experiments and Modeling. The photooxidation of dodecane and subsequent SOA formation is studied using the Caltech Environmental Chamber (11, 12). Dodecane at initial concentration of 34 parts per billion (ppb) in the presence of ammonium sulfate seed particles under dry conditions [relative humidity (RH) < 5%] was oxidized by OH radicals at low concentrations of NO_x typical of nonurban conditions. The kinetic multilayer model of gas-particle interactions in aerosols and clouds (KM-GAP) (13) is used to simulate the evolution of SOA mass, the organic atomic oxygen-to-carbon (O:C) ratio, and particle-size distribution in the chamber experiments (Fig. 1). The model treats the following processes explicitly: gas-phase diffusion, reversible adsorption, bulk diffusion, and chemical reactions in the gas and particle phases. The model also accounts for the loss of gas-phase SVOCs to the chamber Teflon wall (14, 15) based on measurements for representative compounds in separate experiments (*SI Materials and Methods*, *Gas-phase wall loss*, Table S1 and S2). The physical state of the particle bulk is assumed to be semisolid with an average bulk diffusivity of 10^{-12} $cm^2 \cdot s^{-1}$ [a typical value for a semisolid state (16) (*SI Materials and Methods*)], consistent with observations that long-chain alkane-derived SOA particles bounce moderately on the smooth plates of an inertial impactor indicating behavior between that of liquid and glassy particles (17).

In the gas phase, SVOCs resulting from up to five generations of OH oxidation are considered (Fig. 1*A*). Fig 1*B* shows the span of O:C ratio and gas-phase saturation concentrations for the surrogate SVOCs based on the dodecane oxidation mechanism of Yee et al. (11). Some of the fourth generation products have been established to be multifunctional carbonyl compounds, aldehydes, and ketones. The aldehydes can react with hydroperoxide, hydroxyl, and peroxycarboxylic acid groups, forming peroxyhemiacetal (PHA), hemiacetal, and acylperoxyhemiacetal, respectively, in the particle phase (2, 11, 18). Ketone functional

Author contributions: M.S., L.D.Y., and J.H.S. designed research; M.S., L.D.Y., K.A.S., C.L.L., and J.S.C. performed research; M.S., L.D.Y., K.A.S., C.L.L., J.S.C., A.Z., and P.J.Z. analyzed data; M.S., L.D.Y., K.A.S., and C.L.L. wrote the supplement; and M.S., and J.H.S. wrote the paper.

The authors declare no conflict of interest.

This article is a PNAS Direct Submission.

[1]To whom correspondence should be addressed. E-mail: seinfeld@caltech.edu.

This article contains supporting information online at www.pnas.org/lookup/suppl/doi:10.1073/pnas.1307501110/-/DCSupplemental.

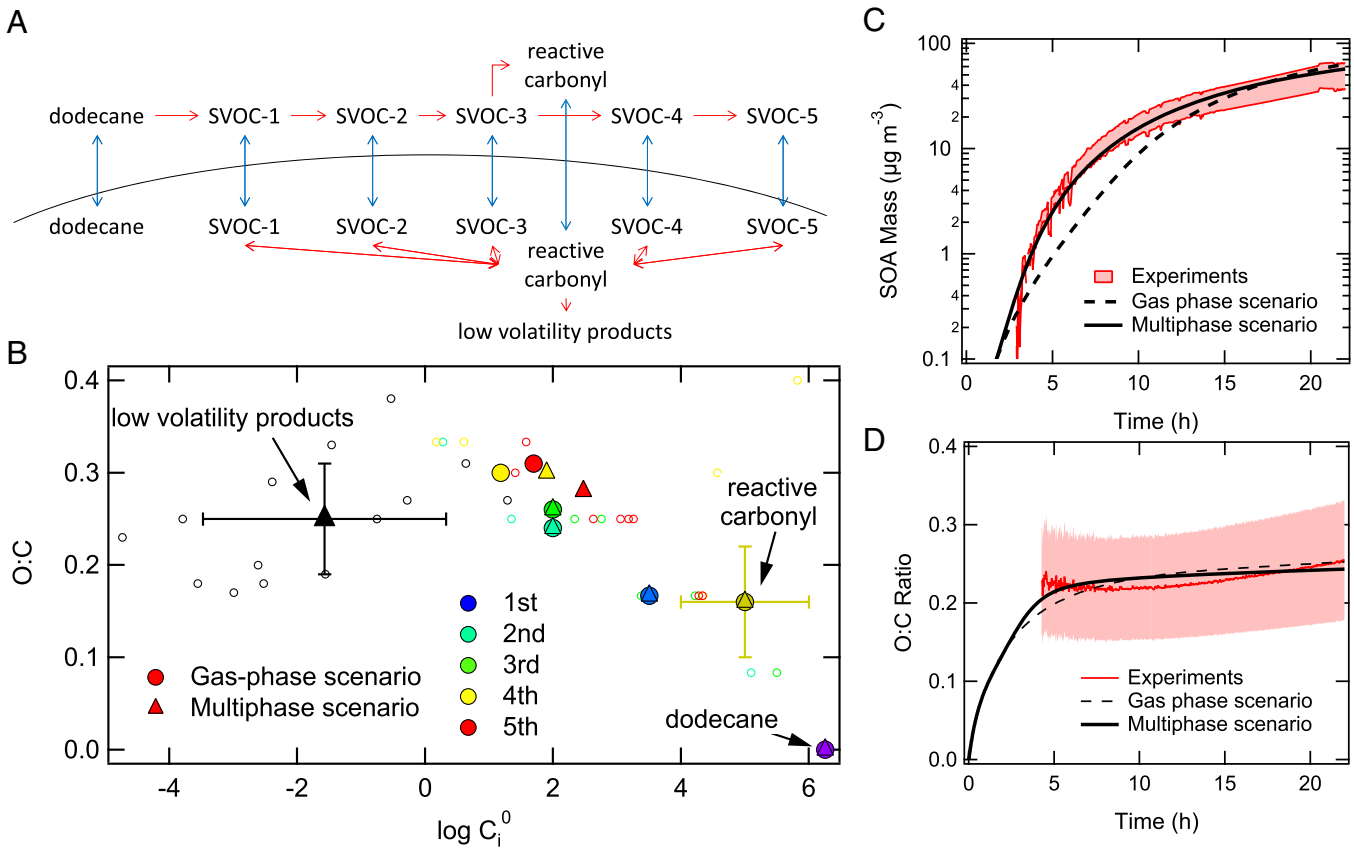

Fig. 1. Modeling secondary organic aerosol formation from dodecane photooxidation. (*A*) Schematic of the mass transport (blue arrows) and chemical reactions (red arrows) in the dodecane SOA system. Multigeneration of SVOCs is considered in the gas phase. The multiphase scenario includes second-order reactions (red double arrows) between reactive carbonyl and SVOCs forming low-volatility products in the particle phase. (*B*) O:C ratios for products of dodecane oxidation vs. their predicted gas-phase saturation concentration (μg·m^{-3}) over the pure (subcooled) liquids (C_i^0). The smaller symbols indicate individual products predicted in the dodecane photooxidation chemical mechanism developed by Yee et al. (11). Color indicates the gas-phase generation in which compound is formed. These compounds include reactive carbonyl compounds (fourth generation). Black symbols indicate particle-phase products. The large solid circles and triangles indicate the surrogate SVOC compounds in the gas-phase and multiphase scenarios, respectively. Measured (red) and modeled SOA mass concentration (*C*) and O:C ratio (*D*) with the gas-phase (dashed line) and multiphase (solid line) scenarios, respectively. The upper and lower red lines in the *C* correspond to upper and lower bound wall loss corrections, respectively. The measured O:C ratio is subject to ±30% uncertainty (12).

groups can react with hydroxyl groups, catalyzed by acids, forming a variety of oligomers (4). These products have significantly lower volatility than their gas-phase precursors, as shown for PHA by the black triangles in Fig. *1B*. We evaluate the potential effect of particle-phase chemistry on SOA formation by simulating two distinct scenarios. In the "multiphase" model scenario, the formation of low-volatility products arising from particle-phase chemistry is considered whereas, in the "gas-phase" scenario, only gas-phase reactions are accounted for. In the kinetic model simulations, the volatility and O:C ratio of each surrogate product are chosen to lie in the range of those of corresponding individual compounds, as shown by the large solid and triangle markers in Fig. 1*B* for the gas and multiphase scenarios, respectively. Note that the O:C ratios of later generation gas-phase and particle-phase products are both ∼0.25. Fig. 1*C* shows the experimental observations of SOA mass concentration for the cases of two limiting particle-wall loss corrections (19, 20): (*i*) wall-deposited particles are assumed to cease interaction with the gas phase (lower red line), and (*ii*) wall-deposited particles are assumed to continue interacting with the gas phase as if they were still suspended (upper red line). Fig. 1*D* shows the measured O:C ratio (12). Both scenarios, gas-phase (dashed lines) and multiphase (solid lines), are able to match the observed SOA mass concentration and O:C ratio within the experimental uncertainties, even though the gas-phase scenario initially underestimates SOA mass for times up to ∼10 h. This result exemplifies the ambiguity that arises in assessing the chemical routes to SOA formation based solely on SOA mass and O:C ratio.

Fig. 2*A* shows the measured evolution of the particle-size distribution. The mean particle diameter grows from ∼60 nm to ∼180 nm over ∼20 h. The simulated size distribution for the gas-phase scenario is shown in Fig. 2*B*. In contrast to the observed size distribution, the gas-phase scenario predicts a broad size distribution that is a characteristic also found for quasi-equilibrium growth mechanism (21), in which the condensed SVOCs equilibrate quickly with the gas phase. When SVOCs equilibrate with the particle population, they tend, on average, to partition to larger particles because of their greater absorption capacity and the reduction in equilibrium vapor pressure over the surface compared with that over smaller particles (the Kelvin effect). By contrast, the simulated number size distribution for the multiphase scenario captures the characteristic narrowing of the measured size distribution (Figs. 2 *C* and *D*, Fig. S1). The evolution of the volume size distribution is also well reproduced by the multiphase scenario (Fig. S2). Evaporation and recondensation of SVOCs tend to be inhibited in this case owing to the formation of low volatility products in the particle phase. The narrowing of the size distribution is characteristic of kinetically limited growth, in which the mass of condensing material is

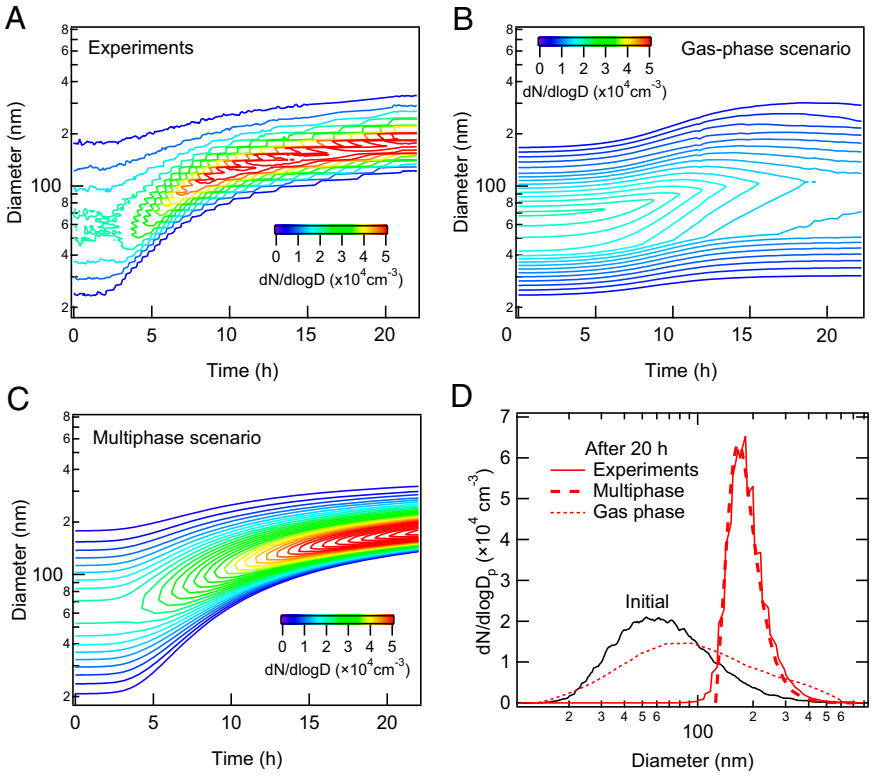

Fig. 2. Evolution of particle number size distribution. Measured (with the upper-bound wall loss correction) (*A*) and modeled by KM-GAP with gas-phase (*B*) and multiphase (*C*) scenarios. (*D*) Initial number size distribution (black) and measured (red solid line) and modeled number size distribution after 20 h in the gas-phase (dotted line) and multiphase (dashed line) scenarios.

distributed proportional to the particle surface area (21, 22). The second-order reaction rate coefficient between reactive carbonyl and SVOCs (k_{BR}), which is estimated to be 12 $M^{-1}{\cdot}s^{-1}$ (2×10^{-20} $cm^3{\cdot}s^{-1}$), is found to be the most sensitive parameter in controlling the evolution of the particle size distribution. The evolution of SOA mass and number size distribution obtained with an initial dodecane concentration of 8 ppb was also modeled well using the same parameters of the multiphase scenario (Fig. S3).

Fig. 3 shows the simulated evolution of the mass concentration ratio of oxidation products in the particle (Fig. 3*A*) and gas phase (Fig. 3*B*) in the multiphase scenario. During the first several hours, the particle phase is dominated by first- to third-generation SVOCs, which are progressively converted to higher generation SVOCs in the gas phase and low volatility products in the particle phase. The contribution of particle-phase products to the total SOA budget is predicted to exceed 60% after ∼5 h. The dominance of low-volatility particle-phase products is consistent with previous studies, in which peroxyhemiacetals were found to be major products in SOA derived from oxidation of alkenes (1-tetradecene) (23, 24), aromatic hydrocarbons (toluene) (25, 26), and monoterpenes (α- and β-pinene) (27).

Fig. 3*C* shows the simulated radial profile of the production rate of low-volatility products along with the evolution of particle radius. The production rate becomes substantial, with a rate of $>2 \times 10^{17}$ $cm^{-3}{\cdot}s^{-1}$ in the surface layer after ∼4 h when SOA mass starts growing (Fig. 1*C*). The particle-phase reactions are predicted to occur mainly at and near the surface, consistent with a product analysis study suggesting that PHA formation should occur mainly at the particle surface (24). Fig. 3*D* shows the measured evolution of gas-phase C_6-carboxylic acid, which is a fourth-generation product and a proxy for the expected formation of aldehydes (11). Aerosol mass spectrometer (AMS) ions at mass-to-charge ratios (m/z) of 183 and 215 are also shown, which are representative fragments from the carbonyl hydroperoxide (CARBROOH; $C_{12}H_{24}O_3$) and its derived PHA (11). The onset of gas-phase aldehyde, particle-phase PHA, SOA mass growth, and production rate of low-volatility products at ∼4 h suggests that the formation of PHA triggers initial SOA growth.

Tridecanal Injection Experiment. To evaluate the hypothesis concerning the role of PHA production in SOA formation, we have conducted an additional chamber experiment with intentional injection of the aldehyde tridecanal (Fig. 4). Dodecane (initial concentration of 239 ppb) was photooxidized for 4 h under low-NO_x and dry conditions in the presence of ammonium sulfate seed particles, at which time chamber UV lights were turned off to halt production of OH radicals, ceasing gas-phase chemistry and SOA growth. After 6 h, injection of 9.5 ppb tridecanal into the chamber led to a rapid increase in organic mass (measured by the AMS) of ∼45 $\mu g{\cdot}m^{-3}$ within 1 h. Simultaneously, the tracer ions for gas-phase CARBROOH decreased and that for particle-phase CARBROOH-derived PHA increased. The same trend was also observed for organic hydroperoxide and its derived PHA (Fig. S4). Direct analysis in real time mass spectrometry (DART-MS) spectra confirm the formation of high molecular mass compounds such as PHA and oligomers (Fig. S5 and Table S3). Note that the observed SOA growth cannot be explained by physical uptake of tridecanal, as its vapor pressure is too high ($C_0 = \sim 10^5$ $\mu g{\cdot}m^{-3}$).

As the observed particle growth is predicted to be essentially a result of the particle-phase reaction, the second-order reaction rate between tridecanal and SVOCs can be estimated to lie in the range 0.3–12 $M^{-1}{\cdot}s^{-1}$ (*SI Materials and Methods, Estimation of the particle-phase reaction rate coefficient*). This range is consistent with the estimated k_{BR} of 12 $M^{-1}{\cdot}s^{-1}$ derived from the

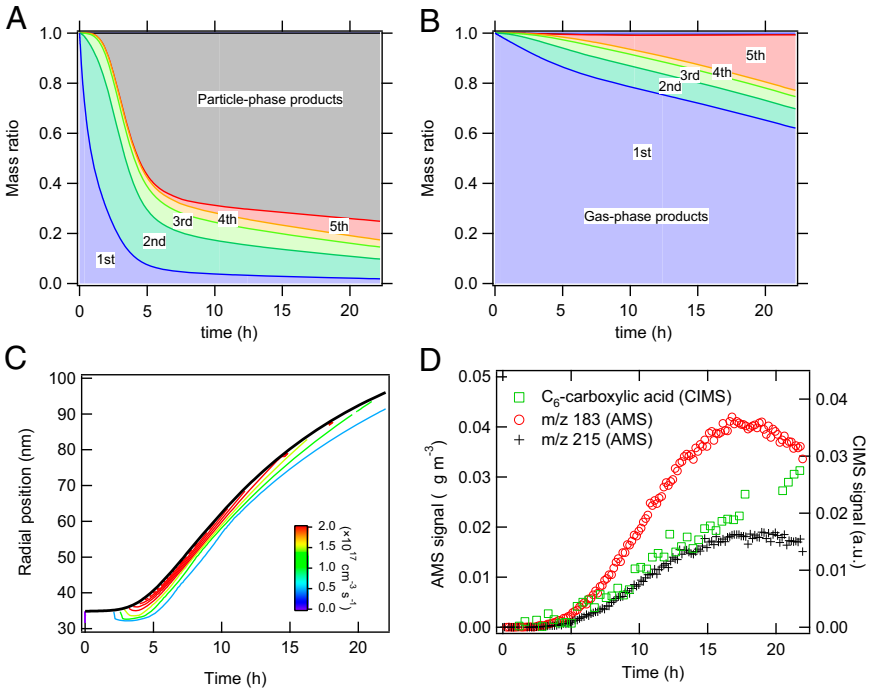

Fig. 3. Relative contribution and distribution of gas-phase and particle-phase reaction products. Mass concentration ratios of multigeneration dodecane gas-phase oxidation products (colored) and particle phase products (gray) in the particle phase (*A*) and the gas phase (*B*), modeled with the multiphase scenario. (*C*) Modeled radial profile of the production rate ($cm^{-3}{\cdot}s^{-1}$) of particle-phase products for an initially 35-nm radius particle. The solid black line indicates the evolution of the particle radius. (*D*) Temporal evolution of a C_6-carboxylic acid (tracer for aldehyde/reactive carbonyl) in the gas phase monitored by the CIMS. Two characteristic tracers of peroxyhemiacetal formation in the particle phase are measured by the AMS at *m/z* 183 ($C_{12}H_{23}O^+$) and *m/z* 215 ($C_{12}H_{23}O_3^+$).

KM-GAP modeling of the dodecane photooxidation experiments. Note that literature values of k_{BR} for uncatalyzed reactions of various hydroperoxides and aldehydes in different solvents range from 10^{-4} to 0.06 $M^{-1}{\cdot}s^{-1}$ (18, 28). The value of k_{BR} inferred from the observations indicates that the reactions must be catalyzed (by two orders of magnitude) by the presence of acids (4, 18, 24) generated in the low-NO_x dodecane mechanism (11). This magnitude of enhancement seems reasonable, as in the case of hemiacetal formation from acetaldehyde plus methanol, the presence of 1 M acetic acid increases the rate constants by a factor of ~250 (18).

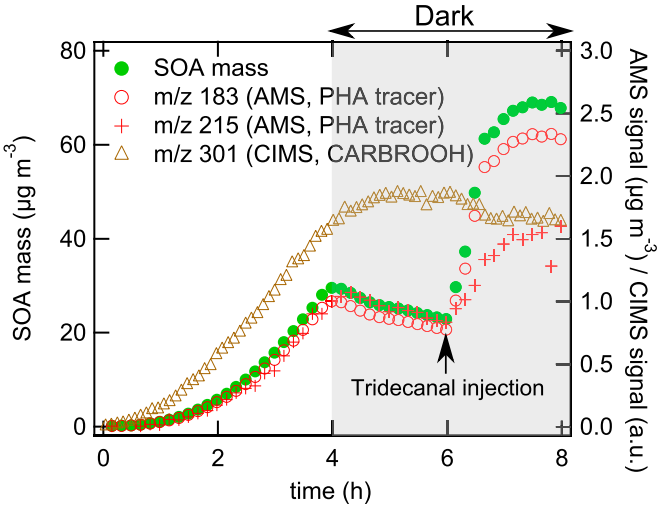

Fig. 4. Intentional aldehyde (tridecanal) injection experiments. SOA mass concentration and carbonyl hydroperoxide (CARBROOH; $C_{12}H_{24}O_3$) signal monitored by CIMS at *m/z* 301 and CARBROOH-derived peroxyhemiacetals monitored by the AMS at *m/z* 183 ($C_{12}H_{23}O^+$) and *m/z* 215 ($C_{12}H_{23}O_3^+$). UV lights are switched off after 4 h, and 9.5 ppb tridecanal is injected to the chamber at 6 h.

Summary and Implications. The results of the current work have a number of implications for SOA models. Although the dynamics of an aerosol size distribution reflects the mechanism of growth (22, 29), we demonstrate here that it provides a key constraint in interpreting laboratory and ambient SOA formation. Aldehyde injection experiments suggest that peroxyhemiacetal formation by heterogeneous reactions between aldehydes and organic hydroperoxides can have a major impact on SOA formation. This work, although carried out specifically for the long chain alkane dodecane, is expected to be widely applicable to other major classes of SOA precursors. SOA consists of a myriad of organic compounds containing carbonyl, hydroxyl, and carboxyl groups (among other functional groups), which can generally undergo heterogeneous/multiphase reactions forming low-volatility products such as oligomers and other high molecular mass compounds (18). The importance of such a peroxyhemiacetal formation pathway depends on the reaction rate constants and concentrations of reactants as well as on particle acidity and hygroscopicity because the reactions can be acid-catalyzed (4, 30, 31) or hydration-based (32), depending on the environmental conditions and particle composition. Heterogeneous reactivity of SOA particles can be regulated by relative humidity and temperature, which will affect particle viscosity and bulk diffusivity (16, 33). If particle-phase chemistry is indeed central to SOA growth in general, the size-resolved SOA formation is better described in terms of kinetically limited condensational growth, rather than solely by thermodynamic equilibrium partitioning (22, 34). Analysis of field and laboratory data on size-distribution

dynamics and heterogeneous chemistry for various SOA precursors and environmental conditions may lead to more robust predictions of chemical composition and particle-size distribution, with relevance to properties such as radiative forcing and cloud condensation nuclei activity.

Materials and Methods

Chamber Experiments. Experiments were carried out in the Teflon reactors in the Caltech Environmental Chamber. Aqueous H_2O_2 solution was evaporated into the chamber, followed by the atomization of an aqueous ammonium sulfate solution generating seed particles, which were subsequently dried. Liquid dodecane was evaporated into the chamber to achieve 34 ppb gas-phase mixing ratio of dodecane. After an hour of mixing, the blacklights were turned on, initiating generation of the OH radical from H_2O_2 photolysis. The gas-phase composition of oxidation products was monitored using a chemical ionization mass spectrometer (CIMS) (11). The particle-phase chemical composition, including the atomic oxygen-to-carbon (O:C) ratio of SOA, was measured by an Aerodyne high-resolution time-of-flight aerosol mass spectrometer (HR-ToF-AMS) (12). In addition, particle-phase chemical composition was analyzed offline using direct analysis in real time mass spectrometry (DART-MS). Particle number size distribution was measured using a cylindrical differential mobility analyzer coupled to a condensation particle counter. More details are available in *SI Materials and Methods*.

Kinetic Modeling. The kinetic multilayer model of gas-particle interactions in aerosols and clouds (KM-GAP) (13) is used for simulations. For size-resolved simulations, the bin method with full-moving size structure is used. KM-GAP consists of a number of compartments and layers in which semivolatile species can undergo mass transport and chemical reactions in the gas and particle phases. The required kinetic parameters for surrogate SVOCs include the gas-phase first-order reaction rate coefficients, the surface accommodation coefficient, the molecular desorption lifetime, gas and bulk diffusion coefficients, and the second-order bulk reaction rate coefficient for the reaction of reactive carbonyl with SVOCs (Table S1 and S2). The dynamics of compound concentrations in the gas and particle phases and of the aerosol size distribution were computed by solving the mass balance, transfer, and reaction rate equations. More details are described in *SI Materials and Methods*.

ACKNOWLEDGMENTS. We thank Xuan Zhang and Matt Coggon for assistance in the experiments. This work was supported by US Department of Energy Grant DE-SC0006626 and National Science Foundation Grant AGS-1057183. M.S. is supported by a Japan Society for the Promotion of Science Postdoctoral Fellowship for Research Abroad.

1. Hallquist M, et al. (2009) The formation, properties and impact of secondary organic aerosol: Current and emerging issues. *Atmos Chem Phys* 9(14):5155–5235.
2. Kroll JH, Seinfeld JH (2008) Chemistry of secondary organic aerosol: Formation and evolution of low-volatility organics in the atmosphere. *Atmos Environ* 42(16): 3593–3624.
3. Jimenez JL, et al. (2009) Evolution of organic aerosols in the atmosphere. *Science* 326(5959):1525–1529.
4. Jang MS, Czoschke NM, Lee S, Kamens RM (2002) Heterogeneous atmospheric aerosol production by acid-catalyzed particle-phase reactions. *Science* 298(5594):814–817.
5. Kalberer M, et al. (2004) Identification of polymers as major components of atmospheric organic aerosols. *Science* 303(5664):1659–1662.
6. Wang L, et al. (2010) Atmospheric nanoparticles formed from heterogeneous reactions of organics. *Nat Geosci* 3(4):238–242.
7. Robinson AL, et al. (2007) Rethinking organic aerosols: semivolatile emissions and photochemical aging. *Science* 315(5816):1259–1262.
8. Presto AA, et al. (2009) Intermediate-volatility organic compounds: A potential source of ambient oxidized organic aerosol. *Environ Sci Technol* 43(13):4744–4749.
9. Lee-Taylor J, et al. (2011) Explicit modeling of organic chemistry and secondary organic aerosol partitioning for Mexico City and its outflow plume. *Atmos Chem Phys* 11(24):13219–13241.
10. Schauer JJ, Kleeman MJ, Cass GR, Simoneit BRT (1999) Measurement of emissions from air pollution sources. 2. C_1 through C_{30} organic compounds from medium duty diesel trucks. *Environ Sci Technol* 33(10):1578–1587.
11. Yee LD, et al. (2012) Secondary organic aerosol formation from low-NO_x photooxidation of dodecane: Evolution of multigeneration gas-phase chemistry and aerosol composition. *J Phys Chem A* 116(24):6211–6230.
12. Craven JS, et al. (2012) Analysis of secondary organic aerosol formation and aging using positive matrix factorization of high-resolution aerosol mass spectra: Application to the dodecane low-NOx system. *Atmos Chem Phys* 12(24):11795–11817.
13. Shiraiwa M, Pfrang C, Koop T, Pöschl U (2012) Kinetic multi-layer model of gas-particle interactions in aerosols and clouds (KM-GAP): Linking condensation, evaporation and chemical reactions of organics, oxidants and water. *Atmos Chem Phys* 12(5): 2777–2794.
14. Matsunaga A, Ziemann PJ (2010) Gas-wall partitioning of organic compounds in a Teflon film chamber and potential effects on reaction product and aerosol yield measurements. *Aerosol Sci Technol* 44(10):881–892.
15. Loza CL, et al. (2010) Characterization of vapor wall loss in laboratory chambers. *Environ Sci Technol* 44(13):5074–5078.
16. Shiraiwa M, Ammann M, Koop T, Pöschl U (2011) Gas uptake and chemical aging of semisolid organic aerosol particles. *Proc Natl Acad Sci USA* 108(27):11003–11008.
17. Saukko E, et al. (2012) Humidity-dependent phase state of SOA particles from biogenic and anthropogenic precursors. *Atmos Chem Phys* 12(16):7517–7529.
18. Ziemann PJ, Atkinson R (2012) Kinetics, products, and mechanisms of secondary organic aerosol formation. *Chem Soc Rev* 41(19):6582–6605.
19. Loza CL, et al. (2012) Chemical aging of m-xylene secondary organic aerosol: Laboratory chamber study. *Atmos Chem Phys* 12(1):151–167.
20. Weitkamp EA, Sage AM, Pierce JR, Donahue NM, Robinson AL (2007) Organic aerosol formation from photochemical oxidation of diesel exhaust in a smog chamber. *Environ Sci Technol* 41(20):6969–6975.
21. Shiraiwa M, Seinfeld JH (2012) Equilibration timescale of atmospheric secondary organic aerosol partitioning. *Geophys Res Lett* 39:L24801.
22. Riipinen I, et al. (2011) Organic condensation: A vital link connecting aerosol formation to cloud condensation nuclei (CCN) concentrations. *Atmos Chem Phys* 11(8): 3865–3878.
23. Tobias HJ, Docherty KS, Beving DE, Ziemann PJ (2000) Effect of relative humidity on the chemical composition of secondary organic aerosol formed from reactions of 1-tetradecene and O_3. *Environ Sci Technol* 34(11):2116–2125.
24. Tobias HJ, Ziemann PJ (2000) Thermal desorption mass spectrometric analysis of organic aerosol formed from reactions of 1-tetradecene and O_3 in the presence of alcohols and carboxylic acids. *Environ Sci Technol* 34(11):2105–2115.
25. Johnson D, Jenkin ME, Wirtz K, Martin-Reviejo M (2004) Simulating the formation of secondary organic aerosol from the photooxidation of toluene. *Environ Chem* 1(3): 150–165.
26. Sato K, Hatakeyama S, Imamura T (2007) Secondary organic aerosol formation during the photooxidation of toluene: NOx dependence of chemical composition. *J Phys Chem A* 111(39):9796–9808.
27. Docherty KS, Wu W, Lim YB, Ziemann PJ (2005) Contributions of organic peroxides to secondary aerosol formed from reactions of monoterpenes with O_3. *Environ Sci Technol* 39(11):4049–4059.
28. Capouet M, et al. (2008) Modeling aerosol formation in alpha-pinene photo-oxidation experiments. *J Geophys Res Atmos* 113(D2):D02308.
29. McMurry PH, Wilson JC (1982) Growth laws for the formation of secondary ambient aerosols: Implications for chemical conversion mechanisms. *Atmos Environ* 16(1): 121–134.
30. Zhao J, Levitt NP, Zhang R (2005) Heterogeneous chemistry of octanal and 2,4-hexadienal with sulfuric acid. *Geophys Res Lett* 32(9):L09802.
31. Iinuma Y, Boge O, Gnauk T, Herrmann H (2004) Aerosol-chamber study of the alpha-pinene/O_3 reaction: Influence of particle acidity on aerosol yields and products. *Atmos Environ* 38(5):761–773.
32. Zhao J, Levitt NP, Zhang R, Chen J (2006) Heterogeneous reactions of methylglyoxal in acidic media: Implications for secondary organic aerosol formation. *Environ Sci Technol* 40(24):7682–7687.
33. Kuwata M, Martin ST (2012) Phase of atmospheric secondary organic material affects its reactivity. *Proc Natl Acad Sci USA* 109(43):17354–17359.
34. Perraud V, et al. (2012) Nonequilibrium atmospheric secondary organic aerosol formation and growth. *Proc Natl Acad Sci USA* 109(8):2836–2841.

Supporting Information

Shiraiwa et al. 10.1073/pnas.1307501110

SI Materials and Methods

KM-GAP Model and Parameters. A kinetic multi-layer model of gas-particle interactions in aerosols and clouds (KM-GAP) (1) is used for simulations. For size-resolved simulations, the bin method with full-moving size structure is used, in which the number concentration of particles in each size bin is conserved but the single particle volumes change (2). The number of size bins is 20 in this study. Coagulation is not considered in the model, as the coagulation timescale of more than a day significantly exceeds the experimental timescale (3, 4). KM-GAP consists of multiple model compartments and layers, respectively: gas phase, near-surface gas phase, sorption layer, surface layer, and a number of bulk layers. KM-GAP treats the following processes explicitly: gas-phase diffusion, gas-surface transport (reversible adsorption), surface-bulk exchange, bulk diffusion, and a selection of chemical reactions in the gas and particle phases. Note that assumptions of instantaneous gas-particle partitioning and homogeneous mixing of the particle bulk, which are often assumed in secondary organic aerosol (SOA) modeling studies (5), were not applied. Surface and bulk layers can either grow or shrink in response to mass transport, which eventually leads to particle growth or shrinkage. Surface-bulk transport and bulk diffusion are treated as mass transport from one bulk layer to the next through first-order transport velocities, which are calculated from the bulk diffusion coefficients (1). As the experiments considered here were conducted under dry conditions, ammonium sulfate is assumed to remain in the form of crystalline seed particles on which SOA condenses. The ammonium sulfate core is represented by one bulk layer, and the organic phase is resolved with 10 bulk layers. Ideal mixing is assumed within the organic phase (mole fraction-based activity coefficients are assumed to be unity), an assumption that is reasonable for an SOA phase formed by the oxidation products of a single parent compound (here dodecane) at conditions of low water content (low relative humidity) (6). Loss of gas-phase semivolatile organic compounds (SVOCs) to the chamber wall (4, 7) is considered using a pseudo-first order gas-phase wall-loss coefficient k_w (see *Gas-phase wall loss* for determination of k_w values). Particle wall loss is not considered in the model; thus, the particle-number concentration stays constant. The dynamics of mass concentrations in the gas and particle phases and of the aerosol size distribution are computed by numerically solving the ordinary differential equations for the mass balance of each model compartment (1).

Five generations of gas-phase oxidation are considered, each generation of which is represented by a surrogate compound. Yee et al. (8) have developed the dodecane low-NO_x gas-phase chemical mechanism based on gas-phase measurements of dodecane photooxidation in conjunction with the Master Chemical Mechanism (MCM, version 3.2) (9). Yee et al. (8) estimated gas-phase saturation concentrations ($\mu g \cdot m^{-3}$) over the pure (subcooled) liquids (C_i^0) for oxidation products predicted by a detailed gas-phase chemical mechanism using the EVAPORATION (Estimation of Vapor Pressure of Organics, Accounting for Temperature, Intramolecular, and Nonadditivity effects) method (10), as shown in the open color circles in Fig. 1*B*. C_i^0 values for surrogate compounds are determined by varying C_i^0 over the predicted range for each generation to fit to the measured SOA mass. The first-order gas-phase reaction rate constants are summarized in Table S1, which is based on the chemical mechanism for dodecane photooxidation developed by Yee et al. (8). Concerning the branching ratio for formation of reactive carbonyl compounds in the fourth generation of gas-phase oxidation, a number of compounds are predicted to contain ketone and aldehyde groups by the chemical mechanism (8); thus, we chose to vary the branching ratio over the range of 0.1–0.9. For the simulations presented in Fig. 1, the value of 0.4 is taken. In the multiphase scenario, particle-phase reactions between SVOCs and reactive carbonyls are considered using the second-order bulk reaction rate coefficient (k_{BR}) as listed in Table S1. k_{BR} is assumed to be the same for all reactions. The k_{BR} value was varied to fit the model to the experimental data, resulting in a value of $k_{BR} = 2 \times 10^{-20}$ $cm^3 \cdot s^{-1}$.

The required kinetic parameters for the SVOCs are listed in Table S2, which includes an estimate for the surface accommodation coefficient on a free substrate (α_s), the molecular desorption lifetime (τ_d), gas and bulk diffusion coefficients (D_g, D_b), and the second-order bulk reaction rate coefficient (k_{BR}) for the reaction of reactive carbonyl with SVOCs. D_g is assumed to be 0.05 $cm^2 \cdot s^{-1}$ (11). Note that the sensitivity studies by varying D_g in the range of 0.02–0.2 $cm^2 \cdot s^{-1}$ revealed that D_g is not critical for describing SOA mass and size distribution, indicating that gas-phase diffusion is not the limiting step in SOA formation. τ_d is assumed to be 1 μs (1). α_s is often assumed to be unity in organic aerosol modeling studies (12). Estimates of the accommodation coefficient of SVOC using thermodenuders have resulted in values in the range of 0.28–0.46 (13). α_s is estimated to be 0.3–0.5 by kinetic modeling (1) of evaporation data of dioctyl phthalate (14). In this study, we assume $\alpha_s = 0.5$. A sensitivity study by varying α_s in the range of 0.1–1 in the multiphase scenario revealed that SOA mass and size distribution are not especially sensitive to the value of α_s, suggesting that surface accommodation is not the limiting step in SOA growth in the present case.

Neither the bulk viscosity nor the bulk diffusivity of dodecane SOA is known. Saukko et al. (15) measured a bounce behavior of SOA particles formed from the oxidation of *n*-heptadecane (a long-chain alkane). At low relative humidity (RH), particles bounced from the plate of an inertial low-pressure impactor, indicating that they are not a liquid (of low viscosity), but the particles did not bounce with the behavior of solid or glassy particles; with a bounce fraction of ~0.5, the *n*-heptadecane SOA particles are deemed to be semisolid. The typical bulk diffusivities of multifunctional organic compounds in semisolid phases range from 10^{-20} to 10^{-10} $cm^2 \cdot s^{-1}$ (16, 17). We assume here that the SOA products from the *n*-dodecane oxidation have similar diffusivities as the *n*-heptadecane SOA. D_b was varied systematically over the given range to fit to the data of SOA mass and size distribution; the optimal value was found to be 10^{-12} $cm^2 \cdot s^{-1}$. Note that, if the particles are assumed to be liquid with D_b in the range of 10^{-10} to 10^{-5} $cm^2 \cdot s^{-1}$, indeed size distribution was not reproduced as well as in the case that the particle is assumed to be semisolid. The most sensitive parameters in fitting SOA mass are the gas-phase saturation concentrations ($\mu g \cdot m^{-3}$) for SVOCs. The second-order bulk reaction rate coefficient k_{BR} is the most critical parameter in controlling the evolution of the particle number size distribution. This finding is understood as this coefficient affects the average vapor pressures of the condensed SOA species via the conversion of higher-volatility monomers to low-volatility dimers and oligomers.

Dodecane Photooxidation Experiments. ***Experimental methods.*** Dodecane photooxidation experiments were conducted in the dual 28 m^3 Caltech Environmental Chambers (3, 18) as described in Yee et al.

(8). The extended OH exposure of more than 22 h was achieved using the experimental chamber protocol of Loza et al. (19). A gas chromatograph with flame ionization detection (GC-FID; Agilent 6890) with an HP-5 column was used to monitor the dodecane decay at 1 h time resolution. A chemical ionization mass spectrometer (CIMS) (20–22) was used for tracking the gas-phase development of several hydroperoxide species, ketones, and acids. The CIMS operated in both positive ionization mode for a mass scan range of 50–200 amu $[M\bullet(H_2O)_n.H]^+$ and negative ionization mode for a mass scan range of 50–300 amu $[M\bullet CF_3O]^-$, $[M\bullet F]^-$, where M is the analyte. NO, NO_x, O_3, temperature, and RH were all monitored. NO and NO_x levels remained below 5 parts per billion (ppb), the lower detection limit of the chemiluminescence analyzer (Horiba; APNA 360), and photochemical simulations (8) confirmed that, at the sufficiently low levels of NO_x, the fate of the alkylperoxy radical (RO_2) is dominated by reaction with HO_2. Initial O_3 levels were 3 ppb, rising to 22 ppb by the end of the experiment. Temperature remained between 296 and 298 K after irradiation began, and RH remained below 5%.

A differential mobility analyzer (TSI Model 3081), coupled with a condensation particle counter (TSI Model 3010), was used for monitoring the particle-size distribution. An Aerodyne high-resolution time-of-flight aerosol mass spectrometer (HR-ToF-AMS) was operated according to protocols described in Yee et al. (8) and Craven et al. (23). Briefly, the HR-ToF-AMS (24) was operated collecting data at 1 min resolution, switching between a higher resolution, lower sensitivity "W" mode and a lower resolution, higher sensitivity "V" mode. Analysis of AMS data were performed according to analysis procedures previously described (24–27). Chamber reactors were flushed for 24 h with purified dry air before each experiment. Then 280 μL of 50% by weight aqueous H_2O_2 solution was injected into a glass trap. The glass trap was submerged in a warm water bath (35–38 °C), and the solution was evaporated by flowing 5 L·min^{-1} of purified dry air through the trap into the chamber. This resulted in ∼4 ppm H_2O_2 concentration in the chamber. A 0.015 M aqueous ammonium sulfate solution was atomized into the chamber until a seed volume of ∼11 μm^3·cm^{-3} was achieved. Next, 9 μL of *n*-dodecane (Sigma-Aldrich) was injected into a glass bulb and evaporated under gentle heating into a 5 L·min^{-1} flow of purified dry air delivered to the chamber, resulting in an initial concentration of 34 ppb. After 1 h of mixing, the blacklights were turned on to initiate photooxidation.

With the same procedure, the photooxidation experiments were also conducted with an initial concentration of dodecane of 8 ppb. The AMS was not available for the 8 ppb experiments. For those experiments, the measured SOA mass and particle size distribution are modeled well using the same parameters of the multiphase scenarios for 34 ppb experiment, as shown in Fig. S3.

Particle wall loss. The upper and lower wall loss corrections bound the amount of aerosol deposited to the Fluorinated ethylene propylene (FEP) Teflon chamber walls during an experiment. To estimate the mass growth rate of wall-deposited particles, the mass growth rate of suspended particles must be determined. We use the Aerosol Parameter Estimation (APE) model described by Pierce et al. (28) for this purpose. The APE model uses the General Dynamic Equation (29) to describe the condensation, coagulation, and wall loss of an aerosol population. The model is initialized with a suspended particle-size distribution at one time step and solves for particle wall loss parameters and a mass growth parameter, F_c (cm·s^{-1}), that produce the best match to the particle size distribution measured at the next time step. In the present case, particle wall loss rate constants are determined in separate particle wall loss experiments (18, 19, 30), and these rate constants are used directly in the model.

Once the mass growth parameters are known, they are applied to particles deposited to the walls. The aerosol General Dynamic Equation also governs deposited particle size distribution behavior, and deposited particles are assumed not to undergo coagulation. The change in the size distribution for deposited particles is governed by

$$\frac{\partial n_w}{\partial t} = \beta(D_p) n_s(D_p,t) - F_c \omega \left[-\frac{1}{D_p^2} n_w(D_p,t) + \frac{1}{D_p} \frac{\partial n_w(D_p,t)}{\partial D_p} \right], \quad \textbf{[S1]}$$

where n_w is the deposited particle size distribution (cm^{-3}), t is time (s), $\beta(D_p)$ is the wall loss rate constant, D_p is the particle diameter (cm), n_s is the suspended particle size distribution (cm^{-3}), and ω is a parameter that describes the extent of gas-particle partitioning for deposited particles. Values for ω range from 0 to 1, with $\omega = 0$ representing no gas-particle partitioning to deposited particles whereas $\omega = 1$ describes gas-particle partitioning to deposited particles identical to that to suspended particles. Here, only the limits (0, 1) for values of ω are considered. To determine the deposited particle size distribution, Eq. **S1** is solved at each size distribution time step using the value of F_c calculated from the APE model at that time step with constant ω. The wall loss corrected particle-size distribution is calculated by summing the suspended and deposited number size distributions. The wall loss corrected SOA volume concentration is calculated from the wall loss corrected size distribution. To calculate the mass of organic aerosol formed, the seed particle volume concentration is subtracted from the wall loss corrected particle volume concentration, and the resulting organic volume concentration is multiplied by a mean particle density, here 1.12 g·cm^{-3}, as determined in a separate nucleation chamber experiment (seed-free), to obtain the organic mass concentration.

Gas-phase wall loss. Gas-phase SVOCs can be absorbed by the Teflon film during the experiments (4, 7). The pseudo-first order gas-phase wall loss coefficient k_w is determined from dark vapor-phase wall loss experiments. Two vapor-phase wall loss experiments were run, using 3,6-octanediol and 2-dodecanone (Sigma-Aldrich), respectively. The hydrocarbon was injected into the reactor, and then the decay was monitored by the CIMS. A first-order wall loss coefficient was calculated from the slope of ln$C$/lnC_o vs. time, where C is the signal for the hydrocarbon and C_o is the hydrocarbon signal 21 min after completion of the hydrocarbon injection (mixing time). Then 10.7 mg of 3,6-octanediol was weighed out into a glass bulb and gently heated while 5 L·min^{-1} of dry purified air flowed through to the reactor. There was slight recondensation on the injection line, leading to incomplete delivery to the reactor. The 3,6-octanediol signal dropped by 39% over 14 h, leading to a first-order fit of $k_w = 9.6 \times 10^{-6}$ s^{-1}. For the 2-dodecanone experiment, 15.5 μL of 2-dodecanone was injected to the chamber, and its signal decayed by 14% over 22 h, resulting in $k_w = 2.2 \times 10^{-6}$ s^{-1}. Due to difficulties in handling these standards for calibration on the CIMS, the suspended concentration after injection could not be verified to match the target concentration based on the injection amount. Without a calibration factor, the presence of rapid vapor-phase wall loss as observed in Matsunaga and Ziemann (7) cannot be ruled out. If this behavior occurs during the injection or mixing period before C_o is defined, the true rates should be higher than those calculated here. Therefore, we refer to the calculated k_w as pseudo-first order. If a confident calibration factor could be established on the CIMS, care would still need to be taken to minimize losses due to recondensation in the injection line so that these losses are not falsely attributed to rapid vapor-phase wall loss in the reactor.

For the KM-GAP simulations, k_w of SVOCs was varied between the measured values (2.2×10^{-6} to 9.6×10^{-6} s^{-1}) assuming that all five generations of SVOCs are characterized by

the same k_w value. It is found that the value of k_w does not affect the evolution of the shape of the size distribution but can lead to a lower modeled SOA mass up to ~30%. For the simulations of dodecane photooxidation, $k_w = 5 \times 10^{-6}$ s^{-1} is assumed.

Tridecanal Injection Experiments. ***Experimental methods.*** The tridecanal injection experiment was run in a 24 m^3 FEP teflon (2 mil) reactor. The same gas- and particle-phase instruments as described in the photooxidation experiments in *Dodecane Photooxidation Experiments, Experimental methods* were used, except that a compact-time-of-flight aerosol mass spectrometer (C-ToF-AMS) (31) was used. Injection protocols were also the same, except loadings were modified to speed up the chemical development and to achieve an organic loading sufficient for offline filter analyses [Direct analysis in real time mass spectrometry (DART-MS)]. Then 280 μL of aqueous H_2O_2 solution (50% by weight) was injected to achieve a starting concentration of ~5 ppm of H_2O_2 in the reactor. The initial *n*-dodecane concentration was 239 ppb as measured by the GC-FID. Throughout the experiment, NO_x levels remained below the lower detection limit of the analyzer, temperature ranged over 21–22.5 °C, and RH remained below 10%.

Photooxidation occurred during the first 4 h of the experiment. The remainder of the experiment was conducted in the dark. After 6 h from the start of irradiation, tridecanal (Sigma-Aldrich) was injected. Then 24.5 mg of tridecanal (assuming no line/wall losses) was delivered to the reactor by evaporating it under gentle heating into a flow of 5 L·min^{-1} of dry purified air for 30 min. Tridecanal concentration was 9.5 (± 2.5) ppb following injection, as measured by the GC-FID. Filter sampling took place after the SOA mass peaked starting at hour 9. A total sample volume of ~1.9 m^3 (2 h at 16 L·min^{-1}) was drawn onto a Teflon filter (47 mm diameter) and analyzed offline using DART-MS.

Estimation of the particle-phase reaction rate coefficient. Tridecanal reacts with SVOCs (e.g., organic hydroperoxides) to form peroxyhemiacetals (PHA) in the particle phase. Thus, the change of the bulk number concentration of PHA $[PHA]_b$ (cm^{-3}) can be described as follows:

$$\frac{d[\mathrm{PHA}]_b}{dt} = k_{BR,Tri}[\mathrm{SVOC}]_b[\mathrm{Tri}]_b, \qquad \textbf{[S2]}$$

where $k_{BR,Tri}$ (cm^3·s^{-1}) is the second-order reaction rate coefficient between tridecanal and SVOCs. As the increase of the total particle mass concentration C_{tot} (μg·m^{-3}) is predicted to be dominated by PHA formation in the present study, its rate of change can be described using the particle mass concentration of PHA C_{PHA}^{PM} (μg·m^{-3} of air):

$$\frac{dC_{tot}}{dt} \approx \frac{dC_{PHA}^{PM}}{dt} = \frac{M_{PHA}}{N_A}\left(10^6 \mu g\ g^{-1}\right)\frac{d[\mathrm{PHA}]_b}{dt} = \frac{M_{PHA}}{N_A}\left(10^6 \mu g\ g^{-1}\right)k_{BR,Tri}[\mathrm{SVOC}]_b[\mathrm{Tri}]_b, \qquad \textbf{[S3]}$$

where M_{PHA} is the molar mass of PHA (~300–400 g·mol^{-1}) and N_A is the Avogadro constant (6.02×10^{23} mol^{-1}). The factor 10^6 is for the unit conversion of g to μg. The average bulk number concentration $[Tri]_b$ (cm^{-3}) and the average particle-phase mass concentration of tridecanal C_{Tri}^{PM} (μg·m^{-3}) can be roughly estimated based on equilibrium gas-particle partitioning theory (32, 33) using its volatility, namely the pure component gas-phase saturation concentration $C_{Tri}^{0} = 1.6 \times 10^5$ μg·m^{-3} (34),

$$[\mathrm{Tri}]_b = \frac{C_{Tri}^{PM}}{M_{Tri}/N_A}\left(10^6 \mu g\ g^{-1}\right) \qquad \textbf{[S4]}$$

$$C_{Tri}^{PM} = \frac{C_{Tri}^{g}}{C_{Tri}^{0}}C_{tot}, \qquad \textbf{[S5]}$$

where M_{Tri} is the molar mass of tridecanal (198 g·mol^{-1}) and C_{Tri}^{g} (μg·m^{-3}) is the gas phase mass concentration of tridecanal. Note that this is an approximation as a concentration gradient can exist due to slow bulk diffusion. The initial tridecanal gas-phase number concentration was measured by the CIMS to be 9.5 (±2.5) ppb, which corresponds to C_{Tri}^{g} = 77 (±20) μg·m^{-3}. $[SVOC]_b$ can be estimated assuming an average molar mass of SVOC (~200–300 g·mol^{-1}), and a certain fraction (10–100%) of the organic particle content is reactive toward aldehydes, resulting in $[SVOC]_b \sim 10^{20}$ to 10^{21} cm^{-3}.

Based on Eq. **S3**, dC_{tot}/dt is constant if $[SVOC]_b$ and $[Tri]_b$ are constant. Indeed, C_{tot} increased linearly from 22 μg·m^{-3} at tridecanal injection at 6 h to 61 μg·m^{-3} at 6.7 h (Fig. 4 of the main text), corresponding to dC_{tot}/dt = 0.017 μg·m^{-3}·s^{-1}. Inserting these values in Eq. **S3**, $k_{BR,Tri}$ can be estimated to be 2×10^{-22} to 2×10^{-20} cm^3·s^{-1} (or 0.12–12 M^{-1}·s^{-1}). This value is in good agreement with the second-order reaction rate coefficient between reactive carbonyl and SVOCs (k_{BR}) estimated by KM-GAP (12 M^{-1}·s^{-1}) in simulating dodecane photooxidation in which different aldehydes and ketones may be relevant reactants.

DART-MS Analysis. Duplicate Teflon filters (PALL Life Sciences; 47 mm diameter, 1.0 μm pore size, Teflon membrane) were used for particle collection from the chamber upon stabilization of the aerosol volume for off-line chemical analysis. Chamber air was pulled through two stainless steel filter assemblies containing two filters for 2 h at rates of 16 and 23 L·min^{-1}, respectively. In the standard chamber filter collection procedure, the upstream filter collected particles, and the downstream filter served to indicate whether breakthrough had occurred or whether gaseous compounds were condensing on the filters. Upon the termination of the collection period, the filters were removed from the assembly with precleaned stainless steel forceps and stored in 20-mL glass vials with Teflon caps, which were sealed with Teflon tape and stored in plastic containers in a freezer maintained at a temperature of −20 °C.

Filters were analyzed by direct analysis in real-time mass spectrometry (DART-MS) using a custom-built DART source (J. L. Beauchamp group, Caltech) interfaced to a Thermo LTQ ion trap mass spectrometer; positive mode ionization was used in this analysis. DART-MS is an ambient ionization method originally developed by Cody et al. (35). It achieves positive ionization through the generation of metastable triplet helium and its reaction with atmospheric water. For the final proton transfer step to occur, the analyte's proton affinity must exceed that of water. SOA samples collected on Teflon filters were analyzed by folding the filter in half with clean stainless steel forceps, and placing the folded filter so the DART stream ablated the aerosol-containing edge. Blank filters and the breakthrough test filters were analyzed as experimental controls. Data were analyzed using the Thermo proprietary software program, Xcalibur.

SOA samples were also extracted in a 1:1 mixture of GC grade heptane and acetone (vol/vol) via sonication. The extracts were dried down by a gentle stream of N_2, then reconstituted in 150 μL of 1:1 mixture of GC grade heptane and acetone (vol/vol) for analysis by GC/MS (Varian Saturn 2200) with a programmed temperature vaporization (PTV) inlet, DB-5MS-UI column (30 m, 0.250 mm, 0.25 μm; Agilent), and electron impact ionization and chemical ionization with methanol. The PTV temperature program was as follows: (*i*) 45 °C, 0.5 min hold; (*ii*) 180 °C min^{-1} ramp to 300 °C; and (*iii*) 300 °C, 46.58 min hold. The oven temperature program was as follows: (*i*) 65 °C, 10 min hold; (*ii*) 10 °C min^{-1} ramp to 300 °C; and (*iii*) 300 °C, 15 min hold.

Table S3 lists major peaks, defined by signal intensity > 5,000 counts for m/z < 400 Da; signal intensity > 1,000 counts for m/z > 400 Da. Proposed formulae are listed for the ions; matches were assigned when the theoretical mass was within 5 mDa of the measured mass. This mass spectrum was acquired using the AccuToF DART-MS, which was mass-calibrated in positive mode by using PEG-600. The ions with m/z above 400 Da that contain nitrogen may be assigned in two ways: (*i*) they may be nitrate-containing compounds, resulting from reaction with the background levels of NO_x in the chamber (<5 ppb); or (*ii*) they may be PHAs or contain peroxide groups, both of which form adducts with ammonia present in trace amounts in laboratory air, and are measured by DART-MS as ammonium adducts ($[M+17]^+$). The low level of NO_x and the lack of smaller mass organonitrates or alcohols suggest that the ammonium adduct option is more likely in this case.

The mass spectra in Fig. S5 were acquired using the experimental DART source in conjuction with the Thermo LTQ ion trap mass spectrometer with unit mass resolution. Fig. S5*A* shows a duplicate sample of dodecane SOA; the significant overlap with the data in Table S3 indicates similar performance across DART ion sources. Fig. S5*B* shows a sample of SOA from the dodecane low-NO_x photooxidation experiment where tridecanal was added in the gas phase to attempt to force oligomerization by PHA formation. The high-resolution AccuToF DART was unavailable for use at the time of the tridecanal experiment, so only unit mass resolution data were obtained for this sample. From Fig. S5*B*, one can observe that different high molecular weight species were formed in the tridecanal experiment, and that the added SOA mass was not simply tridecanal condensing onto the particles (i.e., the spectrum is not dominated by m/z 199), so it must have reacted after uptake.

Fig. S6 is an extracted ion chromatogram (EIC) that compares the m/z 183 signal from the heptane/acetone extracted SOA generated in the tridecanal experiment and in the dodecane photooxidation experiment. The mass loadings for each experiment were different; more mass was on the filter for the dodecane experiment than the tridecanal experiment. The m/z 183 is the AMS tracer for PHA; because the GC/MS was run in EI mode, it has the potential to generate similar ions as the AMS. Fig. S6 demonstrates that, in the tridecanal experiment, different m/z 183-producing compounds (presumably PHA) were generated. There is more variety of m/z 183-producing compounds in the dodecane experiment EIC than in the tridecanal experiment EIC; this observation suggests that the addition of tridecanal drove the oligomer-forming reaction toward a few specific products, creating less diversity than in the dodecane experiment.

1. Shiraiwa M, Pfrang C, Koop T, Pöschl U (2012) Kinetic multi-layer model of gas-particle interactions in aerosols and clouds (KM-GAP): Linking condensation, evaporation and chemical reactions of organics, oxidants and water. *Atmos Chem Phys* 12(5):2777–2794.
2. Jacobson MZ (2005) *Fundamentals of Atmospheric Modeling* (Cambridge Univ. Press, Cambridge), 2nd Ed.
3. Cocker DR, 3rd, Flagan RC, Seinfeld JH (2001) State-of-the-art chamber facility for studying atmospheric aerosol chemistry. *Environ Sci Technol* 35(12):2594–2601.
4. Loza CL, et al. (2010) Characterization of vapor wall loss in laboratory chambers. *Environ Sci Technol* 44(13):5074–5078.
5. Hallquist M, et al. (2009) The formation, properties and impact of secondary organic aerosol: Current and emerging issues. *Atmos Chem Phys* 9(14):5155–5235.
6. Zuend A, Seinfeld JH (2012) Modeling the gas-particle partitioning of secondary organic aerosol: The importance of liquid-liquid phase separation. *Atmos Chem Phys* 12(9):3857–3882.
7. Matsunaga A, Ziemann PJ (2010) Gas-wall partitioning of organic compounds in a Teflon film chamber and potential effects on reaction product and aerosol yield measurements. *Aerosol Sci Technol* 44(10):881–892.
8. Yee LD, et al. (2012) Secondary organic aerosol formation from low-NO_x photooxidation of dodecane: Evolution of multigeneration gas-phase chemistry and aerosol composition. *J Phys Chem A* 116(24):6211–6230.
9. Saunders SM, Jenkin ME, Derwent RG, Pilling MJ (2003) Protocol for the development of the Master Chemical Mechanism, MCM v3 (Part A): Tropospheric degradation of non-aromatic volatile organic compounds. *Atmos Chem Phys* 3(1):161–180.
10. Compernolle S, Ceulemans K, Muller JF (2011) EVAPORATION: A new vapour pressure estimation methodfor organic molecules including non-additivity and intramolecular interactions. *Atmos Chem Phys* 11(18):9431–9450.
11. Bilde M, Svenningsson B, Monster J, Rosenorn T (2003) Even-odd alternation of evaporation rates and vapor pressures of C3-C9 dicarboxylic acid aerosols. *Environ Sci Technol* 37(7):1371–1378.
12. Riipinen I, et al. (2011) Organic condensation: A vital link connecting aerosol formation to cloud condensation nuclei (CCN) concentrations. *Atmos Chem Phys* 11(8):3865–3878.
13. Saleh R, Khlystov A, Shihadeh A (2012) Determination of evaporation coefficients of ambient and laboratory-generated semivolatile organic aerosols from phase equilibration kinetics in a thermodenuder. *Aerosol Sci Technol* 46(1):22–30.
14. Vaden TD, Imre D, Beránek J, Shrivastava M, Zelenyuk A (2011) Evaporation kinetics and phase of laboratory and ambient secondary organic aerosol. *Proc Natl Acad Sci USA* 108(6):2190–2195.
15. Saukko E, et al. (2012) Humidity-dependent phase state of SOA particles from biogenic and anthropogenic precursors. *Atmos Chem Phys* 12(16):7517–7529.
16. Mikhailov E, Vlasenko S, Martin ST, Koop T, Pöschl U (2009) Amorphous and crystalline aerosol particles interacting with water vapor: Conceptual framework and experimental evidence for restructuring, phase transitions and kinetic limitations. *Atmos Chem Phys* 9(2):9491–9522.
17. Shiraiwa M, Ammann M, Koop T, Pöschl U (2011) Gas uptake and chemical aging of semisolid organic aerosol particles. *Proc Natl Acad Sci USA* 108(27):11003–11008.
18. Keywood MD, Varutbangkul V, Bahreini R, Flagan RC, Seinfeld JH (2004) Secondary organic aerosol formation from the ozonolysis of cycloalkenes and related compounds. *Environ Sci Technol* 38(15):4157–4164.
19. Loza CL, et al. (2012) Chemical aging of m-xylene secondary organic aerosol: Laboratory chamber study. *Atmos Chem Phys* 12(1):151–167.
20. Paulot F, et al. (2009) Isoprene photooxidation: New insights into the production of acids and organic nitrates. *Atmos Chem Phys* 9(4):1479–1501.
21. St Clair JM, McCabe DC, Crounse JD, Steiner U, Wennberg PO (2010) Chemical ionization tandem mass spectrometer for the in situ measurement of methyl hydrogen peroxide. *Rev Sci Instrum* 81(9):094102–094106.
22. Crounse JD, Paulot F, Kjaergaard HG, Wennberg PO (2011) Peroxy radical isomerization in the oxidation of isoprene. *Phys Chem Chem Phys* 13(30):13607–13613.
23. Craven JS, et al. (2012) Analysis of secondary organic aerosol formation and aging using positive matrix factorization of high-resolution aerosol mass spectra: Application to the dodecane low-NOx system. *Atmos Chem Phys* 12(24):11795–11817.
24. DeCarlo PF, et al. (2006) Field-deployable, high-resolution, time-of-flight aerosol mass spectrometer. *Anal Chem* 78(24):8281–8289.
25. Allan JD, et al. (2004) A generalised method for the extraction of chemically resolved mass spectra from Aerodyne aerosol mass spectrometer data. *J Aerosol Sci* 35(7): 909–922.
26. Aiken AC, DeCarlo PF, Jimenez JL (2007) Elemental analysis of organic species with electron ionization high-resolution mass spectrometry. *Anal Chem* 79(21):8350–8358.
27. Aiken AC, et al. (2008) O/C and OM/OC ratios of primary, secondary, and ambient organic aerosols with high-resolution time-of-flight aerosol mass spectrometry. *Environ Sci Technol* 42(12):4478–4485.
28. Pierce JR, et al. (2008) Constraining particle evolution from wall losses, coagulation, and condensation-evaporation in smog-chamber experiments: Optimal estimation based on size distribution measurements. *Aerosol Sci Technol* 42(12):1001–1015.
29. Seinfeld JH, Pandis SN (2006) *Atmospheric Chemistry and Physics: From Air Pollution to Climate Change* (Wiley, New York).
30. Ng NL, et al. (2007) Secondary organic aerosol formation from m-xylene, toluene, and benzene. *Atmos Chem Phys* 7(14):3909–3922.
31. Drewnick F, et al. (2005) A new time-of-flight aerosol mass spectrometer (TOF-AMS): Instrument description and first field deployment. *Aerosol Sci Technol* 39(7):637–658.
32. Pankow JF (1994) An absorption model of gas-particle partitioning of organic-compounds in the atmosphere. *Atmos Environ* 28(2):185–188.
33. Donahue NM, Robinson AL, Stanier CO, Pandis SN (2006) Coupled partitioning, dilution, and chemical aging of semivolatile organics. *Environ Sci Technol* 40(8): 2635–2643.
34. Weast RC (1982) *Handbook of Chemistry and Physics* (CRC, Boca Raton, FL).
35. Cody RB, Laramée JA, Durst HD (2005) Versatile new ion source for the analysis of materials in open air under ambient conditions. *Anal Chem* 77(8):2297–2302.

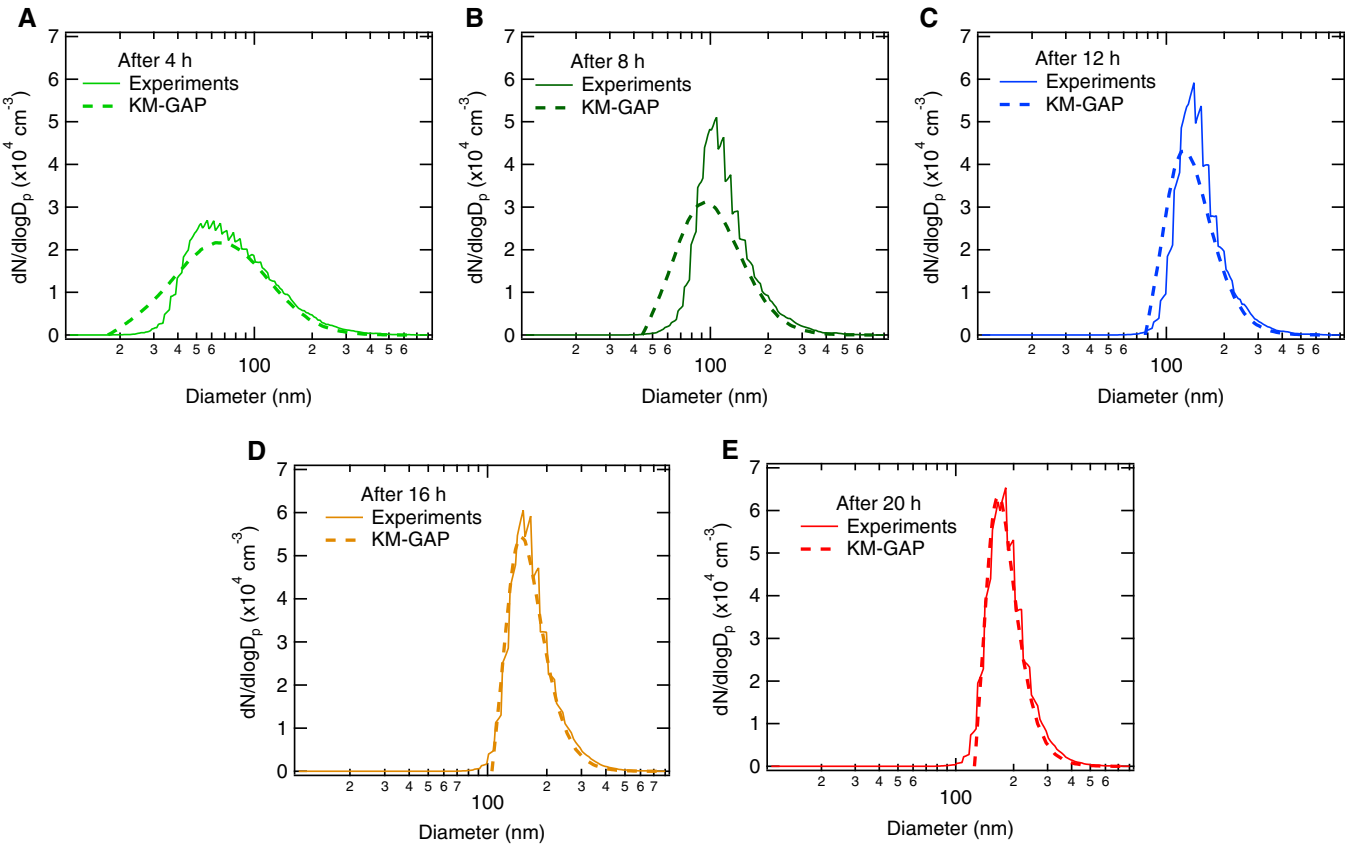

Fig. S1. Experimental (with the upper-bound wall loss correction) and modeled number size distribution (dN/dlogD) by KM-GAP with the multiphase scenario after (*A*) 4 h, (*B*) 8 h, (*C*) 12 h, (*D*) 16 h, and (*E*) 20 h.

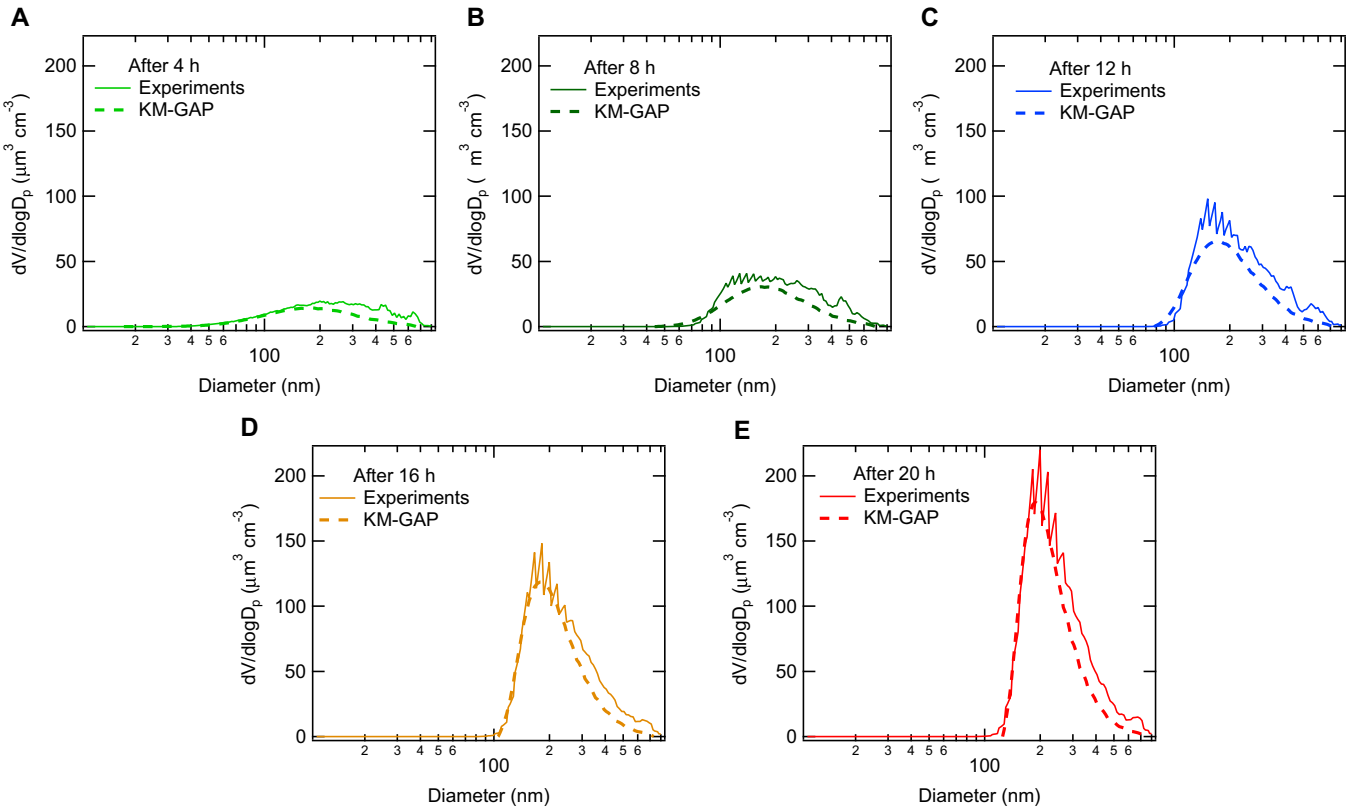

Fig. S2. Experimental (with the upper-bound wall loss correction) and modeled volume size distribution (dV/dlogD) by KM-GAP with the multiphase scenario after (*A*) 4 h, (*B*) 8 h, (*C*) 12 h, (*D*) 16 h, and (*E*) 20 h.

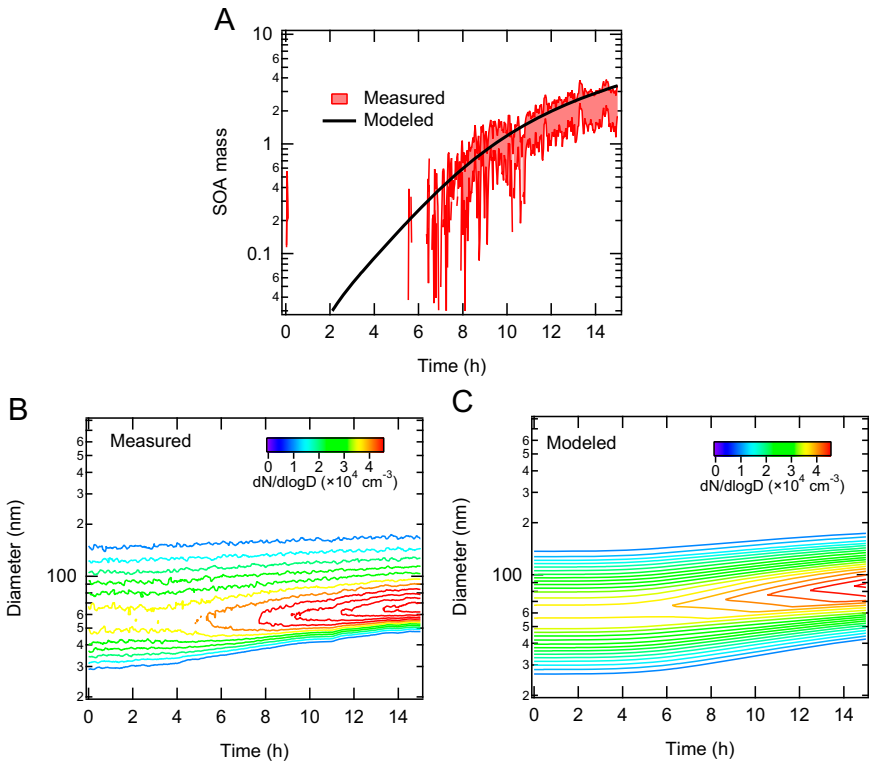

Fig. S3. Modeling SOA formation from dodecane photooxidation. Initial concentration of dodecane was 8 ppb. SOA mass and size distribution is simulated by KM-GAP using the same kinetic parameters of the multiphase scenario used for modeling photooxidation of 34 ppb dodecane (Tables S1 and S2). (*A*) Measured and modeled SOA mass. The extent of the red lines corresponds to upper and lower bound wall loss corrections. (*B*) Measured particle number size distribution with upper-bound wall loss correction. (*C*) Modeled particle number size distribution.

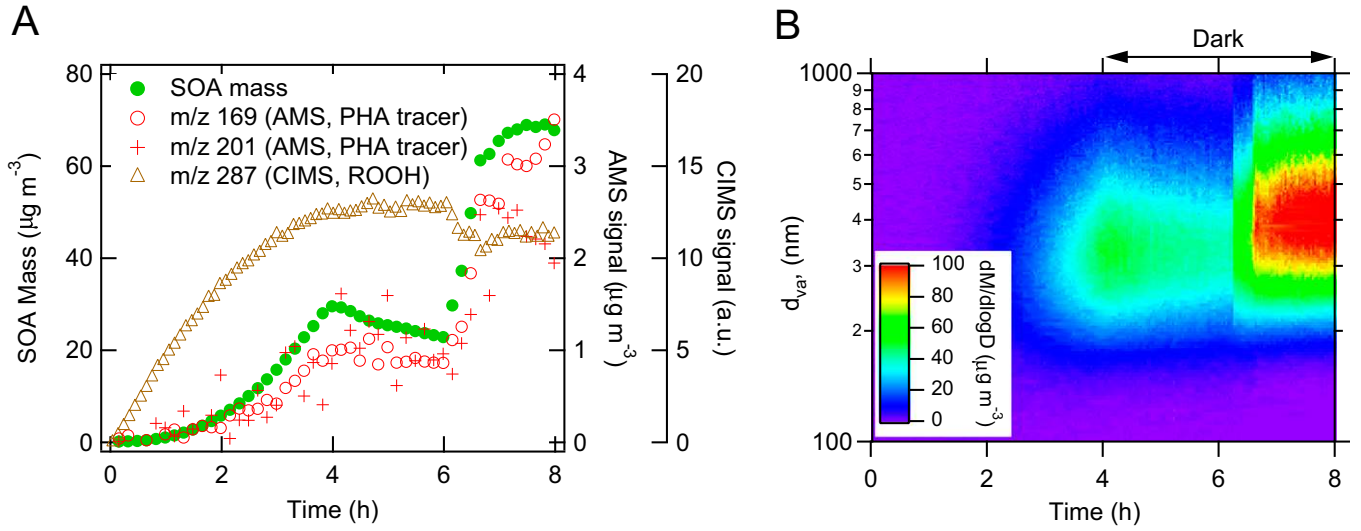

Fig. S4. Intentional aldehyde (tridecanal) injection experiments. Lights are switched off after 4 h, resulting in a net loss of SOA mass due to chamber wall deposition. After 6 h, tridecanal is injected to the chamber. (*A*) SOA mass, organic hydroperoxide ROOH ($C_{12}H_{26}O_2$) signal monitored by CIMS at *m/z* 287 and *m/z* 169 and *m/z* 201 ions measured by the C-ToF-AMS, which are tracers for ROOH-derived PHA. (*B*) Organic aerosol mass size distribution measured by the C-ToF-AMS, showing the growth of mean particle diameter from ~300 nm to ~400 nm due to tridecanal injection.

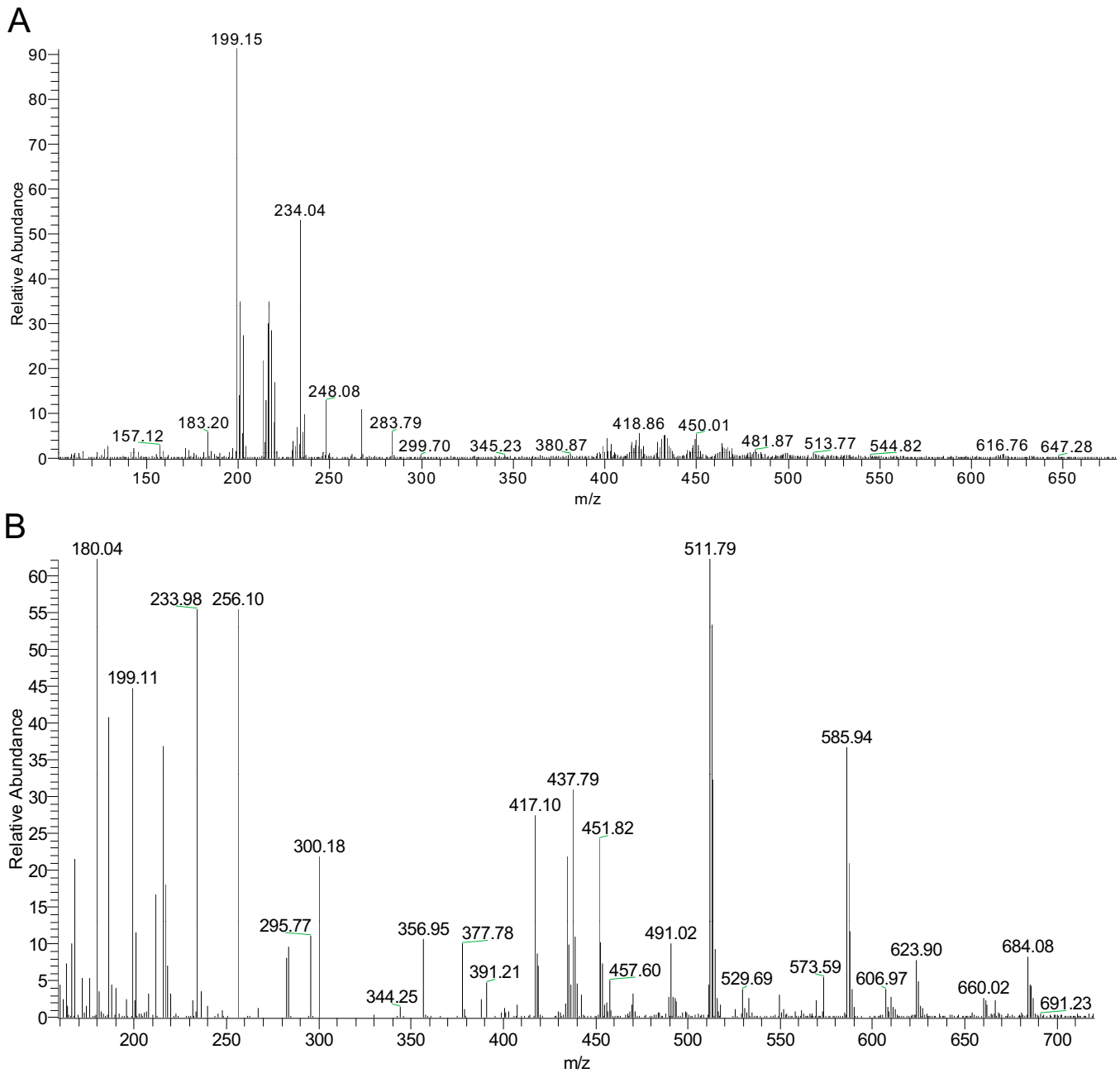

Fig. S5. DART-MS spectrum of SOA formed by photooxidation of dodecane (*A*) and that of SOA formed in tridecanal injection experiments (*B*).

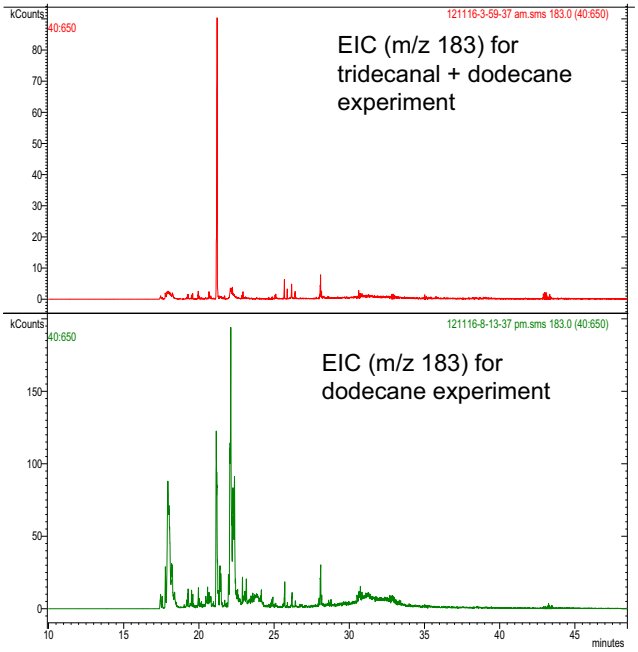

Fig. S6. Extracted ion chromatogram (EIC) that compares the *m/z* 183 signal from the heptane/acetone extracted SOA generated in the tridecanal experiment (*Upper*) and in the dodecane photooxidation experiment (*Lower*).

Table S1. Gas-phase and particle-phase chemistry considered in KM-GAP

Reaction	Reaction rate coefficient
Gas phase	
dodecane → SVOC-1	2.64×10^{-5} s^{-1}
SVOC-1→ SVOC-2	1.71×10^{-5} s^{-1}
SVOC-2→ SVOC-3	1.32×10^{-4} s^{-1}
SVOC-3→ (1 - β) SVOC-4 + β reactive carbonyl	1.85×10^{-4} s^{-1}
SVOC-4→ SVOC-5	1.85×10^{-4} s^{-1}
Particle phase	
SVOC-1 + reactive carbonyl → low volatility products	2×10^{-20} $cm^3 \cdot s^{-1}$
SVOC-2 + reactive carbonyl → low volatility products	2×10^{-20} $cm^3 \cdot s^{-1}$
SVOC-3 + reactive carbonyl → low volatility products	2×10^{-20} $cm^3 \cdot s^{-1}$
SVOC-4 + reactive carbonyl → low volatility products	2×10^{-20} $cm^3 \cdot s^{-1}$
SVOC-5 + reactive carbonyl → low volatility products	2×10^{-20} $cm^3 \cdot s^{-1}$

Gas-phase reactions are considered using the first-order conversion rate coefficients. In the multiphase scenario, particle-phase reactions are considered using the second-order reaction rate coefficient.

Table S2. Estimated kinetic parameters for the surrogate SVOCs in the KM-GAP simulations

Parameters	Description	Value
$\alpha_{s,0}$	Surface accommodation coefficient on a free substrate	0.5
τ_d	Desorption lifetime	1 μs
D_b	Bulk diffusion coefficient	10^{-12} $cm^2 \cdot s^{-1}$
D_g	Gas diffusion coefficient	0.05 $cm^2 \cdot s^{-1}$

Table S3. Major peaks in DART mass spectrum for dodecane low-NO_x SOA

m/z, Da	Intensity, counts	Proposed formula
127.15	6,253.34	$C_8H_{15}O^+$
141.16	9,527.53	$C_9H_{17}O^+$
155.17	9,916.25	$C_{10}H_{19}O^+$
183.19	10,1521.10	$C_{12}H_{23}O^+$
197.16	69,729.89	$C_{12}H_{21}O_2^+$
199.18	52,161.82	$C_{12}H_{23}O_2^+$
213.15	26,890.18	$C_{12}H_{21}O_3^+$
401.36	36,11.87	$C_{24}H_{49}O_4^+$
416.37	3,794.30	$C_{24}H_{50}O_4N^+$
430.35	4,076.51	$C_{24}H_{48}O_4N^+$
446.35	2,134.07	$C_{24}H_{48}O_6N^+$
460.34	1,223.03	$C_{24}H_{46}O_7N^+$